Numerical study of spray-induced turbulence using industrial fire-mitigation nozzles

Guodong Gai, Abdellah Hadjadj, Sergey Kudriakov, Stephane Mimouni, Olivier Thomine

energies

MDPI

Article

Numerical Study of Spray-Induced Turbulence Using Industrial Fire-Mitigation Nozzles

Guodong Gai [1,2], Abdellah Hadjadj [2,*], Sergey Kudriakov [1], Stephane Mimouni [3] and Olivier Thomine [4]

1 DES-DM2S-STMF, CEA, Université Paris-Saclay, 91191 Gif-sur-Yvette, France; guodong.gai@outlook.fr (G.G.); sergey.kudriakov@cea.fr (S.K.)
2 Institute for Applied Sciences, INSA Rouen Normandie, Clean Combustion Laboratory, CORIA UMR 6614 CNRS, 76000 Rouen, France
3 EDF R&D, Fluid Dynamics Power Generation and Environment, 78401 Chatou, France; stephane.mimouni@edf.fr
4 Aix Marseille University, LIS UMR 7020 CNRS, F-13397 Marseille, France; olivier.thomine@univ-amu.fr
* Correspondence: abdellah.hadjadj@insa-rouen.fr

Abstract: A numerical investigation of the spray-induced turbulence generated from industrial spray nozzles is carried out to better understand the roles of the nozzle spray on the fires or explosions in different accidental scenarios. Numerical simulations are first validated against experimental data in the single nozzle case using the monodisperse and polydisperse assumption for droplet diameters. The polydispersion of the nozzle spray is proven to be necessary to correctly predict the gas and droplet velocities. The turbulent kinetic energy has dominant values inside the spray cone, decreases rapidly with the vertical distance from the spray nozzle, and is strongly affected by the spray droplet diameter. On the contrary, the integral length scale is found to have high values outside the spray cone. Two interacting sprays injected from different nozzles are then investigated numerically using the validated polydisperse model. The water sprays generated from such industrial nozzles can generate turbulence of high intensity in the near-nozzle region, and this intensity decreases with the distance from the nozzles. A better understanding of the turbulence generated by the spray system can be beneficial for the evaluation of several important phenomena such as explosion enhancement. The guideline values obtained from this investigation of single and double nozzles can be useful for large-scale numerical simulations.

Keywords: spray nozzle; spray-induced turbulence; polydisperse spray; turbulence intensity

Citation: Gai, G.; Hadjadj, A.; Kudriakov, S.; Mimouni, S.; Thomine, O. Numerical Study of Spray-Induced Turbulence Using Industrial Fire-Mitigation Nozzles. *Energies* **2021**, *14*, 1135. https://doi.org/10.3390/en14041135

Academic Editor: Jiro Senda

Received: 13 January 2021
Accepted: 10 February 2021
Published: 20 February 2021

1. Introduction

Water spray systems are commonly used as emergency devices for fire mitigation purposes in gas processing plants [1], power plants, and offshore platforms [2]. These systems play essential roles in the prevention of severe industrial accidents, such as explosions of hydrogen or other gas fuels [3]. Different flame propagation regimes may exist during the explosion, such as fast deflagration or detonation, depending on the fuel, water steam concentration, as well as ambient pressure and temperature distribution [4]. Various experimental and numerical studies show that the spray systems can have effective mitigation effects on the flame propagation as a result of water droplet evaporation [5,6]. However, the explosion enhancement can also be observed in some experimental studies, due to the spray-generated turbulence in the gas mixture [7]. Thus, an estimation of the turbulence intensity induced by the water spray is needed to evaluate the overall mitigation or enhancement ability of the water spray during accidental explosions.

Spray- or particle-induced turbulence has been an active research field for several decades [8–13]. The presence of spray droplets or particles in the gas can disturb and change the intrinsic turbulence topology of the carrier flow, which is known as turbulence modulation [14]. Several important factors arise that contribute to the turbulence

modulation such as [14,15]: droplet surface, inertia, response, and mass loading. For the case where the carrier phase has a non-zero intrinsic turbulence intensity, the presence of a particle or droplet cloud may have two opposite effects: turbulence attenuation or enhancement [16]. Some criteria are proposed to distinguish between these two opposite effects, such as the length scale ratio [17], the particle momentum number Pa [18], etc. For the system without intrinsic turbulence, the spray injection can directly generate turbulent fluctuations in the gas system.

Numerical evaluations of the turbulent intensity induced by an industrial fire mitigation water spray are scarcely available in the literature. Many factors are involved in the physical modeling, such as the water flow rate, droplet size distribution, injection velocity, etc. These factors are usually coupled and have different values depending on the nozzle types. The water spray generated from an industrial nozzle has a polydisperse nature. Spray droplets directly generated from the nozzle can have diameters varying from 10 µm to 1000 µm [19,20]. Spray nozzles are often placed in linear or circular rows in the dome of a building, as shown in Figure 1. The interaction of the spray droplets generated from different nozzles can be important, leading to the droplet collision, coalescence, etc. [21,22]. This might change the droplet size distributions, as well as the turbulent parameters in the spray interaction zone. Far from the spray nozzle, the typical value of the spray droplet volume fraction is reported to be $\alpha = \mathcal{O}(10^{-4})$ in industrial applications [23], for which the collisions of the droplets can be neglected [24]. For simplicity, solid particles are often used instead of water droplets in many experimental and numerical investigations [25–30]. Compared to water droplets, solid particles are easier to control and have less complicated interaction mechanisms.

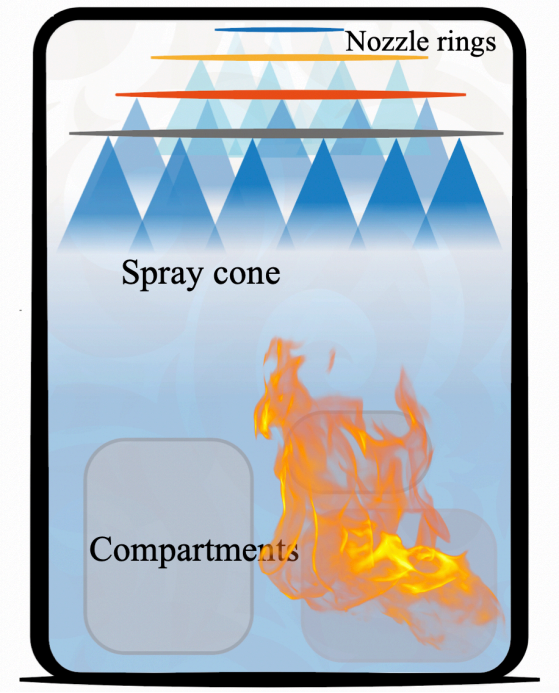

Figure 1. A sketch of the spray system for fire mitigation in an industrial building.

In terms of the numerical simulation of the spray-/particle-induced turbulence, different approaches exist according to the geometrical scale of the problem. Spray injection of very small scales can be simulated using highly-resolved Direct Numerical Simulations (DNSs) [31]. For a variety of engineering applications, the Large Eddy Simulation (LES) models are widely applied [32] for fuel spray injection in engines of a geometry scale of $\mathcal{O}$ (10 cm). However, the industrial fire mitigation water sprays have much larger geometries ($\mathcal{O}$ (1–10 m)) than the fuel sprays in combustion. Moreover, these two approaches can hardly be applied directly in engineering applications of large-scale geometries as a result

of important computational costs. An example of the large-scale simulations can be hydrogen explosions in a nuclear containment building (volume $V = 10^4 \sim 10^5$ m^3) or offshore facilities (volume $V = 10^5 \sim 10^6$ m^3). The smallest grid sizes for these problems can be around $\Delta x \approx \mathcal{O}$ (10 cm), and the direct application of these highly-resolved turbulence models, involving the action of spray and spray-flame interaction, can give erroneous results. The description of spray-induced turbulence in the current commercial engineering code is mostly based on empirical correlations where several factors are user-defined using a set of experimental data and are strongly case-dependent [33]. In this study, we try to use the Reynolds-Averaged Navier–Stokes (RANS) models to evaluate the turbulence generated from one single and two interacting industrial spray nozzles in order to find guideline values for the turbulence intensity in large-scale simulations. The RANS models are widely used for the evaluation of turbulence in many industrial applications [34]. Important parameters are investigated here such as the turbulence kinetic energy and the integral length scale of turbulence.

The objectives of this paper are threefold: (i) evaluation using RANS models of spray-induced turbulence; (ii) investigation of the effects of the spray polydispersion model on the spray-induced turbulence intensity; (iii) qualitative study of the turbulence induced by two interacting sprays generated from two separate nozzles. Section 2 gives the basic assumptions and governing equations of the numerical modeling; Section 3 presents the numerical investigations on the single nozzle spray, containing the mesh grid choice, code validation, as well as the simulation results for both the monodisperse and polydisperse spray of a single nozzle; the study of two interacting sprays is carried out and presented in Section 4; finally, conclusions and perspectives are given in Section 5.

2. Numerical Modeling

2.1. Modeling Assumptions

The following assumptions and simplifications are made in the numerical simulations: (i) the spray droplets are considered to be inert, spherical, rigid particles with constant heat capacity and a uniform temperature distribution; (ii) the volume fraction of the particles is relatively small so that the collision between particles is neglected; (iii) the viscous drag forces and gravity are supposed to act on the particles. The Basset force is neglected, since the particle-to-gas density ratio is high $\mathcal{O}$ (10^3) and the acceleration of particles by the gas flow is small [35]. It is assumed that the particles do not spin; thus, the Magnus force is neglected.

2.2. Governing Equations

The NEPTUNE_CFD code is a Navier–Stokes solver developed jointly by EDF (Électricité de France) and CEA (Commissariat à l'Énergie Atomique et aux Énergies Alternatives) for three-dimensional multi-fluid flows [36,37]. Different turbulence models are implemented in this solver such as the k-ε model, the R_{ij}-ε model, etc. NEPTUNE_CFD relies on a finite volume discretization and can use various mesh types (tetra- or hexa-hedral) for different flow regimes: steady/unsteady, compressible/incompressible, laminar/turbulent.

The governing equations for the two-phase system in Neptune_CFD consist of mass, momentum, and energy conservation laws. The mass conservation equation can be expressed as [38]:

$$\frac{\partial}{\partial t}(\alpha_\kappa \overline{\rho}_\kappa) + \nabla \cdot (\alpha_\kappa \overline{\rho}_\kappa \overline{V}_\kappa) = \Gamma_\kappa, \quad \kappa = l, g, \tag{1}$$

where α_κ denotes the volume fraction of the phase κ, $\overline{\rho}_\kappa$ is the mass density, $\overline{V}_\kappa$ is the local mean velocity of the phase κ, Γ_κ is the interphase mass transfer rate, and l and g denote the liquid and gas phases, respectively.

The momentum conservation gives:

$$\frac{\partial}{\partial t}(\alpha_\kappa \overline{\rho}_\kappa \overline{V}_\kappa) + \nabla \cdot (\alpha_\kappa \overline{\rho}_\kappa \overline{V}_\kappa^2) = -\alpha_\kappa \nabla \overline{p} + M_\kappa + \alpha_\kappa \overline{\rho}_\kappa f_g + \nabla \cdot [\alpha_\kappa (\overline{\tau}_\kappa + \overline{\tau}_\kappa^T)], \quad \kappa = l, g, \tag{2}$$

where $\overline{p}$ is the gas pressure, f_g the gravity acceleration, M_κ the interphase momentum transfer term, and $\overline{\tau}_\kappa$, $\overline{\tau}_\kappa^T$ denote the viscous and Reynolds stress tensors, respectively [39].

The total enthalpy conservation has the expression:

$$\frac{\partial}{\partial t}\left[\alpha_\kappa \overline{\rho}_\kappa \left(\overline{h}_\kappa + \frac{\overline{V}_\kappa^2}{2}\right)\right] + \nabla \cdot \left[\alpha_\kappa \overline{\rho}_\kappa \left(\overline{h}_\kappa + \frac{\overline{V}_\kappa^2}{2}\right)\overline{V}_\kappa\right] = \alpha_\kappa \frac{\partial \overline{p}}{\partial t} + \alpha_\kappa \overline{\rho}_\kappa f_g \overline{V}_\kappa + \Gamma_\kappa \left(\overline{h}_{\kappa,int} + \frac{\overline{V}_\kappa^2}{2}\right) + q_\kappa A_{int} + q_{wk} - \nabla \cdot [\alpha_\kappa(\overline{q}_\kappa + \overline{q}_\kappa^T)]. \quad (3)$$

where h_κ stands for the phase-averaged specific enthalpy for the phase κ, $\overline{h}_{\kappa,int}$ the interfacial-averaged enthalpy, and Γ_κ and $q_\kappa A_{int}$ denote the interfacial transfer of mass and heat, respectively. q_{wk} is the wall-to-fluid heat transfer flux term,and the turbulent heat fluxes in phase κ are represented by $\overline{q}_\kappa$ and $\overline{q}_\kappa^T$, respectively. The flow quantities to resolve are α_κ, ρ_κ, V_κ, and h_κ. More discussions about this two-phase model and turbulent closure laws of different terms can be found in [36,40].

The k-ε turbulence model is used in this study for the description of the gas turbulence. The turbulent variables solved are the turbulent kinetic energy k and the turbulent dissipation rate ε, with the k equation:

$$\overline{\rho}_g \frac{\partial k}{\partial t} + div\left[\overline{\rho}_g \overline{V}_g k - \left(\mu_g + \frac{\mu_t}{\sigma_k}\right)\overrightarrow{grad}\ k\right] = \mathcal{P} + \mathcal{G} - \overline{\rho}_g \varepsilon + k div(\overline{\rho}_g \overline{V}_g), \quad (4)$$

The equation for ε reads:

$$\overline{\rho}_g \frac{\partial \varepsilon}{\partial t} + div\left[\overline{\rho}_g \overline{V}_g \varepsilon - \left(\mu_g + \frac{\mu_t}{\sigma_\varepsilon}\right)\overrightarrow{grad}\ \varepsilon\right] = C_{\varepsilon 1}\frac{\varepsilon}{k}[\mathcal{P} + (1 - C_{\varepsilon 3})\mathcal{G}] - \overline{\rho}_g C_{\varepsilon 2}\frac{\varepsilon^2}{k} + \varepsilon div(\overline{\rho}_g \overline{V}_g), \quad (5)$$

where $\mathcal{P}$ is the shear stress production term:

$$\mathcal{P} = -\overline{\rho}_g R_{i,j}\frac{\partial \overline{V}_{g,i}}{\partial x_j} \quad (6)$$

$\mathcal{G}$ represents the gravity term:

$$\mathcal{G} = \frac{1}{\overline{\rho}_g}\frac{\mu_t}{\sigma_t}\frac{\partial \overline{\rho}_g}{\partial x_i} g_i \quad (7)$$

The eddy viscosity is:

$$\mu_t = \overline{\rho}_g C_\mu \frac{k^2}{\varepsilon} \quad (8)$$

with the constants $C_\mu = 0.09$; $C_{\varepsilon 1} = 1.44$; $C_{\varepsilon 2} = 1.92$; $\sigma_k = 1$; $\sigma_\varepsilon = 1.3$; and $C_{\varepsilon 3} = 1$.

3. Study of a Single Spray Nozzle

3.1. Spray Nozzle

A nozzle commonly used for industrial fire mitigation applications, the nozzle SPRACO 1713A (ref. 373.084.17.BN), shown in Figure 2a [41], is considered. This ramp bottom nozzle can be applied for gas cooling and mixing, dust suppression, etc. The spray generated from the nozzle has the shape of a hollow cone, as shown in Figure 2b. The axial distance from nozzle is denoted as h, while R represents the radial distance from the spray central line. Spray droplets from the nozzle have diameters ranging from 50 µm to 1000 µm with a mean Sauter diameter of 300 µm, with a mass injection rate of 1 kg/s.

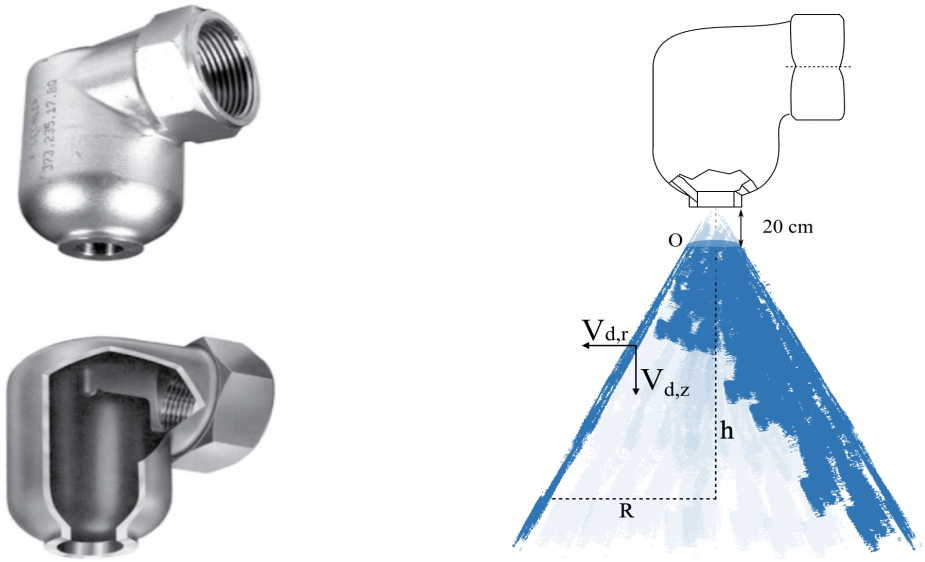

(**a**) (**b**)

Figure 2. (**a**) Ramp bottom nozzle and its section view [41]; (**b**) hollow cone spray with fine droplets. *h*, the vertical distance from the nozzle; *R*, the radial distance from the spray central line; *O*, the numerical injection plane.

3.2. Geometry, Mesh, and Spray Characteristics

The numerical geometry is a cuboid with a size of $3 \times 3.5 \times 3.5$ m^3, representing a quarter of the spray domain, as shown in Figure 3. A spray injection zone is refined around the nozzle central line as depicted in Figure 3a. Symmetric boundary conditions are set on the two vertical surfaces crossed by the centerline of the spray nozzle, shown in yellow in Figure 3a. Wall conditions are set to the other boundaries of the geometry for the gas phase. The bottom of the geometry is set to be a free outlet of the droplets. Different mesh sizes are used in the injection region ranging from $\Delta x = 3$ cm to $\Delta x = 0.67$ cm. An example of the mesh grid is illustrated in Figure 3b.

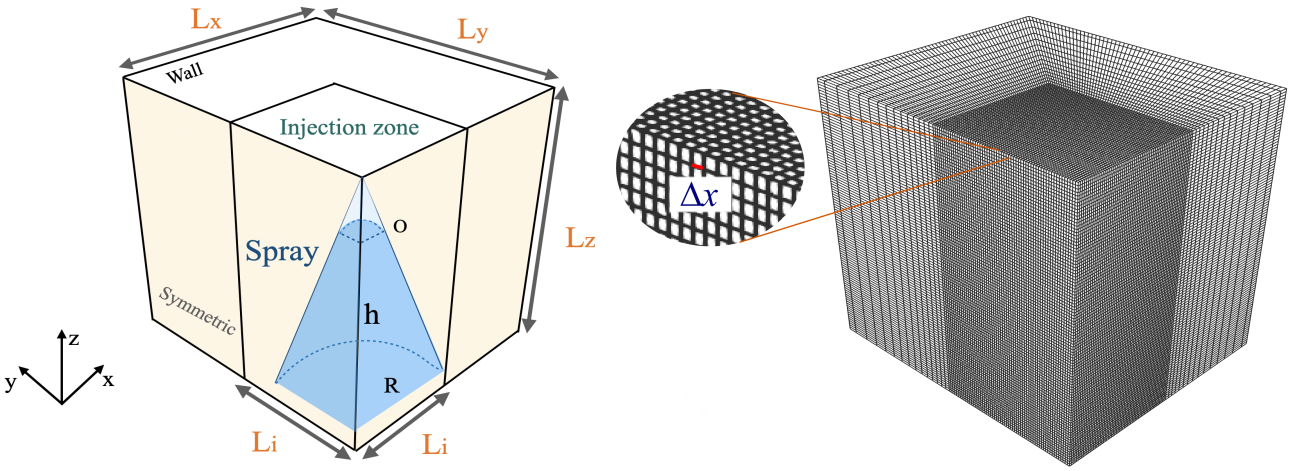

(**a**) (**b**)

Figure 3. Geometry and mesh grid of a single spray nozzle: (**a**) a sketch of the geometry and spray nozzle position; (**b**) a grid of mean mesh size $\Delta x = 1.5$ cm in the injection zone $L_i = 1.5$ m; $L_x = 3.5$ m, $L_y = 3$ m, and $L_z = 3.5$ m; with *O* the numerical injection plane; symmetric and wall boundary conditions highlighted.

Table 1. Particles with different diameters in the polydisperse spray [21].

Particle Class	Diameter (μm)
1	55
2	166
3	277
4	388
5	500
6	611
7	722
8	833
9	944

In the numerical simulations, the primary atomization of the water ligaments out of the nozzle is not considered. The spray droplets are considered to be spherical, solid particles, which are injected at a distance $h = 20$ cm from the nozzle with initial axial and radial velocities obtained from experimental measurements [42,43]. The droplets are injected in a circular ring between $R = 8$ cm and $R = 15$ cm. In order to simplify the simulation, the deformation, breakup, evaporation, and coalescence of the droplets are not considered. Two different spray models are implemented and compared in this section: monodisperse and polydisperse models for the droplet diameter distribution.

In the monodisperse case, the spray droplets share a uniform diameter of 300 μm with an injection mass flow rate of 1 kg/s. The initial axial and radial velocities of the droplets are 17.7 m/s and 7.6 m/s, respectively. In the polydisperse case, the droplets are divided into nine classes, each having different diameters (55 μm, 166 μm, 277 μm, 388 μm, 499 μm, 611 μm, 722 μm, 833 μm, and 944 μm), as shown in Table 1. The injection velocities of the nine different classes of droplets are determined by experimental measurements.

3.3. Simulation Convergence

3.3.1. Mesh Size Effects

The mesh convergence study is performed using the monodisperse spray model for the grids of different mean mesh sizes in the injection region, ranging from $Deltax = 0.67$ cm to $Deltax = 2.5$ cm, as shown in Figure 4. The evolutions of the turbulent kinetic energy as a function of radial distance R are presented in Figure 4a. The convergence of k with the mean mesh size can be seen more clearly in Figure 4c, where one can see that k tends to converge when the mean mesh size becomes smaller than $\Delta x = 1$ cm. Figure 4b shows the axial gas velocity evolutions for different mesh sizes. The droplet and gas velocities, as well as the droplet volume fractions are noted to be less sensitive to the variation of the mesh sizes.

Considering the computational cost, the mesh grid of a mean size of $\Delta x = 1.5$ cm in the spray injection region is used in the following simulations for both the mono- and poly-dispersion cases. From Figure 4c, with $\Delta x = 1.5$ cm, one can have a good order of magnitude of the turbulence kinetic energy k.

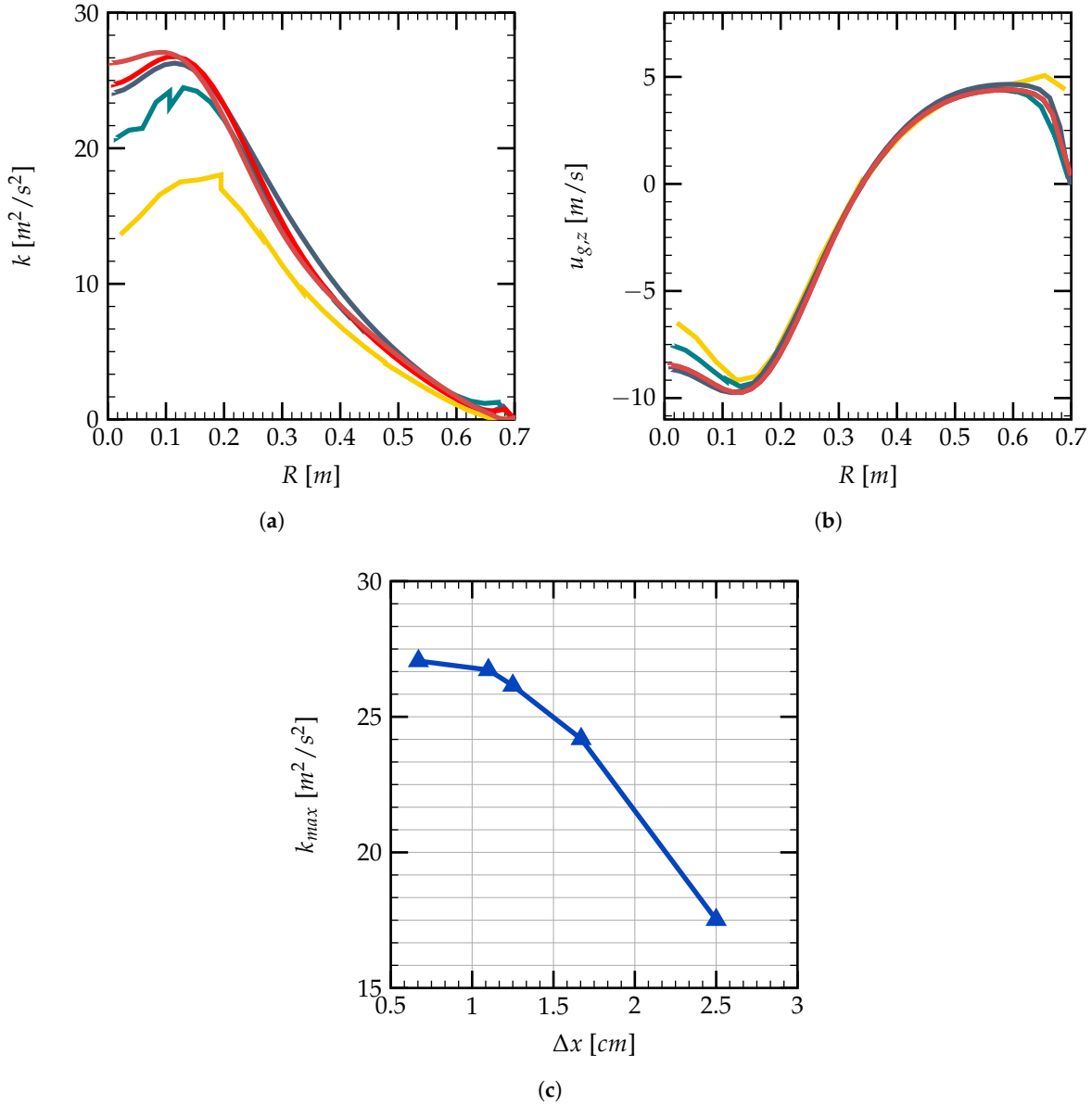

Figure 4. Mesh convergence of different flow parameters as a function of the radial distance from the center R at plane $h = 60$ cm; results of the mean mesh size $\Delta x = 2.5$ cm (—), $\Delta x = 1.67$ cm (—), $\Delta x = 1.25$ cm (—), $\Delta x = 1.11$ cm (—), and $\Delta x = 0.67$ cm (—); (**a**) turbulence kinetic energy k, (**b**) axial gas velocity $u_{g,z}$, and (**c**) the mesh convergence tendency for k_{max} as a function of mean mesh size Δx at plane $h = 60$ cm (—▲—).

3.3.2. Time Convergence

The temporal convergence of k and gas axial velocity is presented in Figure 5. Three numerical point probes are set inside the spray cone to record the evolution of the temporal gas properties. These results are obtained with the monodisperse spray for a calculation time $t = 10$ s with time step $\Delta t = 0.001$ s in a refined grid of mean mesh size $\Delta x = 1.5$ cm.

Figure 5a gives the temporal evolution of the axial gas velocity $u_{g,z}$ for three probe positions, having vertical coordinates of $h = 0.5$ m, 1.5 m, and 2.3 m from the nozzle, respectively. One can see that steady states are obtained very quickly after about 1.5 s of injection for the monodisperse spray. The evolutions of turbulent kinetic energy k also show a quasi-steady state after 1 s, as shown in Figure 5b. Generally, we observe a time convergence for these numerical simulations for a simulation time of 10 s.

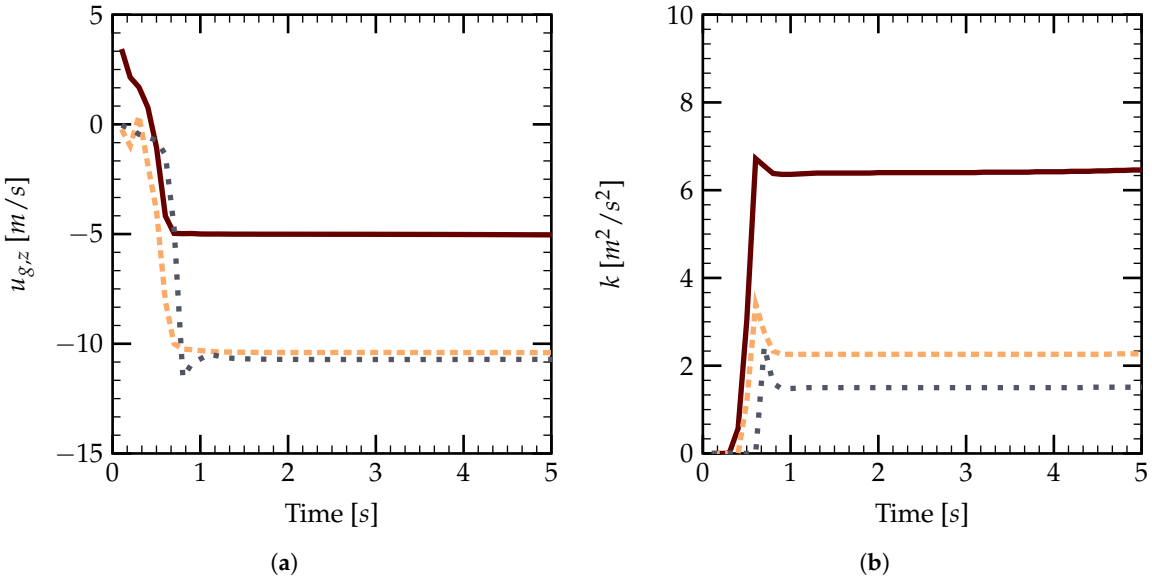

Figure 5. Time convergence of the axial gas velocity $u_{g,z}$ and the turbulent kinetic energy k (m^2/s^2), with $\Delta x = 1.5$ cm, $\Delta t = 1$ ms: Position 1 ($h = 0.5$ m) (——), Position 2 ($h = 1.5$ m) (- - -), and Position 3 ($h = 2.3$ m) (· · ·); (**a**) vertical gas velocity and (**b**) turbulent kinetic energy as a function of time.

3.4. Code Validation

We begin with the validation of the Neptune_CFD code on the velocity of the gas and droplets using the measurements of CALISTexperiments [42,43]. The results of the numerical simulations of the single nozzle spray performed in the work of Foissac et al. [21] are also used as references.

3.4.1. Monodisperse Spray

The validation of the monodisperse case is performed for $t = 10$ s using the grid of mean mesh size $\Delta x = 1.5$ cm, as presented in Figure 6. Figure 6a shows the droplet velocity at different vertical distances $h = 20$ cm, 40 cm, 60 cm, and 95 cm as a function of axial distance R. One can see that the current calculations have a good agreement with the reference numerical simulations of [21] for the axial velocity of droplets. However, the tendency of the droplet velocity given by the numerical simulations is not correct compared to the experimental measurements. This is due to the fact that the monodisperse assumption using a mean value for all spray droplet diameters is not sufficient to predict the dynamics of a real spray.

Figure 6b gives the radial velocity evolution of the droplets at different vertical distances from the spray nozzle h. The numerical calculations can give a rough estimation of the order of magnitude of the experimental results. However, the tendency of the velocity is quite different. The monodisperse assumption is too strong for the simulation of a real spray.

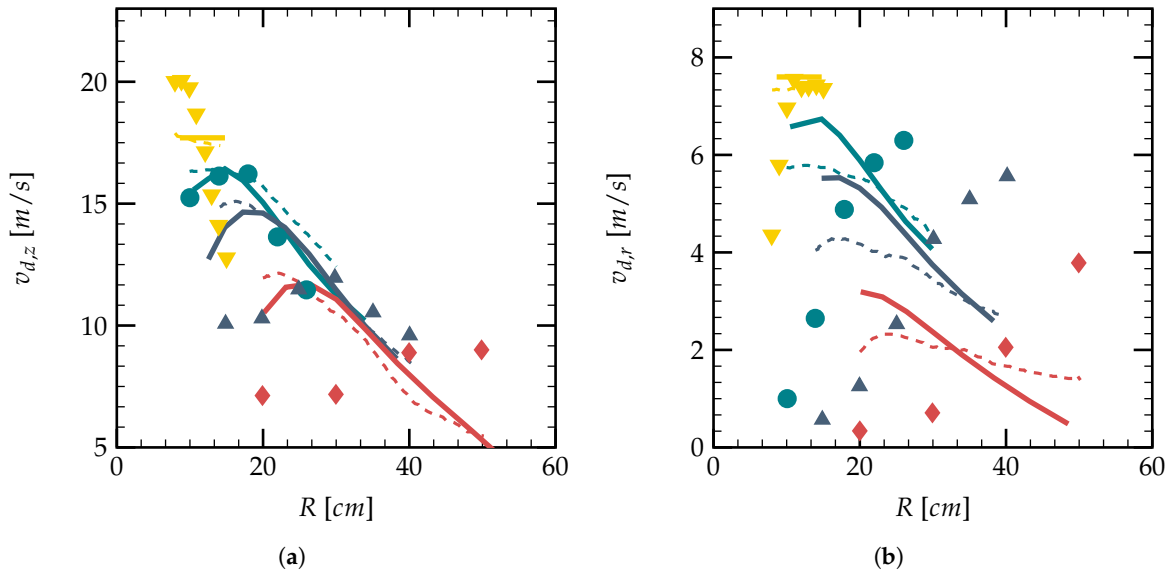

Figure 6. Validation of the droplet velocity at different vertical positions as a function of the radial distance from the center R for a monodisperse spray; (**a**) axial velocity $v_{d,z}$ and (**b**) radial velocity $v_{d,r}$. Experimental measurements at $h = 20$ cm, (▼), $h = 40$ cm (●), $h = 60$ cm (▲), $h = 95$ cm (♦); numerical simulation of [21] at $h = 20$ cm (- - -), $h = 40$ cm (- - -), $h = 60$ cm (- - -), $h = 95$ cm (- - -); current simulation at $h = 20$ cm (——), $h = 40$ cm (——), $h = 60$ cm (——), $h = 95$ cm (——).

3.4.2. Polydisperse Spray

For the polydisperse spray modeling, we have nine different diameters for the droplets, each of which has its own velocity behavior after injection. The mean velocity of all classes of droplets $\bar{v}_d$ can be a representative quantity. Two definitions can be reasonable in this context, either averaged by the volume fraction of each droplet class or averaged by the number of droplets in a given calculation cell. In this study, the number-averaged spray velocity is used for the polydisperse spray. It is emphasized that the cells with a very small quantity ($\alpha_{tot} < 1 \times 10^{-6}$) of droplets are neglected during the calculations of the mean velocity.

Figure 7a shows the mean axial velocity of droplets at different positions along the z axis. One can note that the numerical results have similar behaviors for vertical distances $h < 60$ cm compared to the experimental measurements. Even though the results for $h = 95$ cm give the opposite tendency, one can still have the same order of magnitude for the axial velocities at different radial distances. Compared to the experimental measurements, the current numerical results for the vertical droplet velocity can have a mean relative error of 3.3 % for $h = 20$ cm, 7.6 % for $h = 40$ cm, 12.88 % for $h = 60$ cm, and 27 % for $h = 95$ cm. The relative error increases with the vertical distance of measurement.

The evolutions of the radial components of the mean droplets' velocity are presented in Figure 7b. The relative errors for the droplet radial velocities in the polydisperse spray are larger than the axial velocities. The current numerical results have the same order of magnitude as the experimental results and the numerical results of Foissac [21]. For $h = 20$, 60, and 95 cm, the tendency of the radial velocity matches the experimental data.

Comparing Figure 7 to Figure 6, one can deduce that the consideration of the spray polydispersion can significantly improve the estimation accuracy on the different components of the droplet velocities. Comparing to the former study, we have numerical results of similar accuracy with a less dense mesh grid. The good estimation of both the droplet and gas dynamics is essential for the determination of the turbulence intensity induced by the water spray.

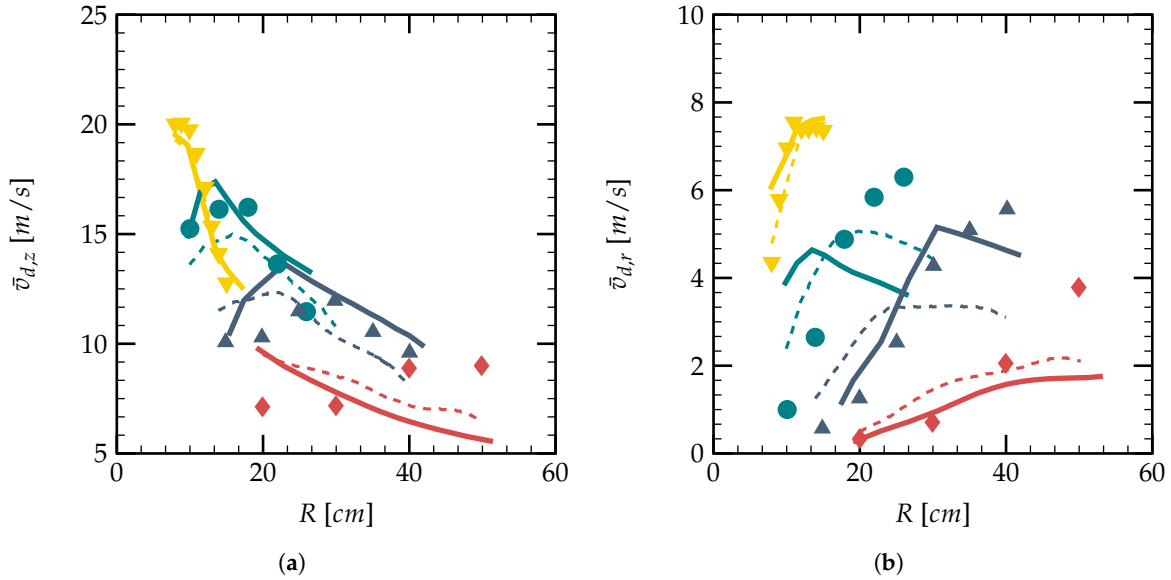

Figure 7. Validation of the droplet velocity at different vertical positions as a function of the radial distance from the center R for a polydisperse spray; (**a**) mean axial velocity $\bar{v}_{d,z}$ and (**b**) mean radial velocity $\bar{v}_{d,r}$. Experimental measurements at $h = 20$ cm, (▼), $h = 40$ cm (●), $h = 60$ cm (▲), $h = 95$ cm (◆); Numerical simulation of [21] at $h = 20$ cm (- - -), $h = 40$ cm (- - -), $h = 60$ cm (- - -), $h = 95$ cm (- - -); current simulation at $h = 20$ cm (——), $h = 40$ cm (——), $h = 60$ cm (——), $h = 95$ cm (——).

3.5. Turbulent Properties of the Monodisperse Spray

Figure 8 shows the spatial distribution of droplet volume fraction α_{tot} and turbulent kinetic energy k for the monodisperse spray injected from a single nozzle. One can see a side view of the droplet volume fraction distribution on the XZplane with $y = 0.05$ m, in Figure 8a. The droplets of diameter 300 µm form a hollow spherical cone after being injected. Then, the radial velocity decreases, and the spray cone has a constant diameter far from the spray nozzle. The turbulent kinetic energy is noted to have high values inside this spray cone, as shown in Figure 8b. With an increasing vertical distance from the spray nozzle, the turbulent kinetic energy k decreases from 8 m^2/s^2 near the nozzle to 1 m^2/s^2 at $h = 2$ m.

3.6. Turbulent Properties of the Polydisperse Spray

Figure 9 presents the numerical results of α_{tot} and k on the XZ plane at $y = 0.05$ m for $t = 10$ s. The same mesh grid is used in the simulations for Figures 8 and 9. One can see the total liquid volume fraction distribution in Figure 9a. Large droplets are noted to be dominant on the outer rim of the spray cone, whereas the small ones are retained on the inner side of the spray.

Comparing to the monodisperse case, the spray cone is larger in the polydisperse spray. The spatial distribution of the turbulent kinetic energy k is presented respectively in Figure 9b. Comparing to Figure 9a, we can find that the region where k has high values is located inside the spray cone, which is the same for the turbulent dissipation rate ε. The turbulence intensity of the air outside the spray cone is less affected by the injection of the spray, which is similar to the monodisperse spray case, as depicted in Figure 8.

Figure 10 shows the distribution of turbulence integral length scale L_t and turbulent kinetic energy k on the XY plane at $h = 1.5$ m. The integral length scale L_t is noted to have high values in the near-field outside the region of the spray cone. Inside the spray cone, L_t is relatively small and increases with the vertical distance from the nozzle.

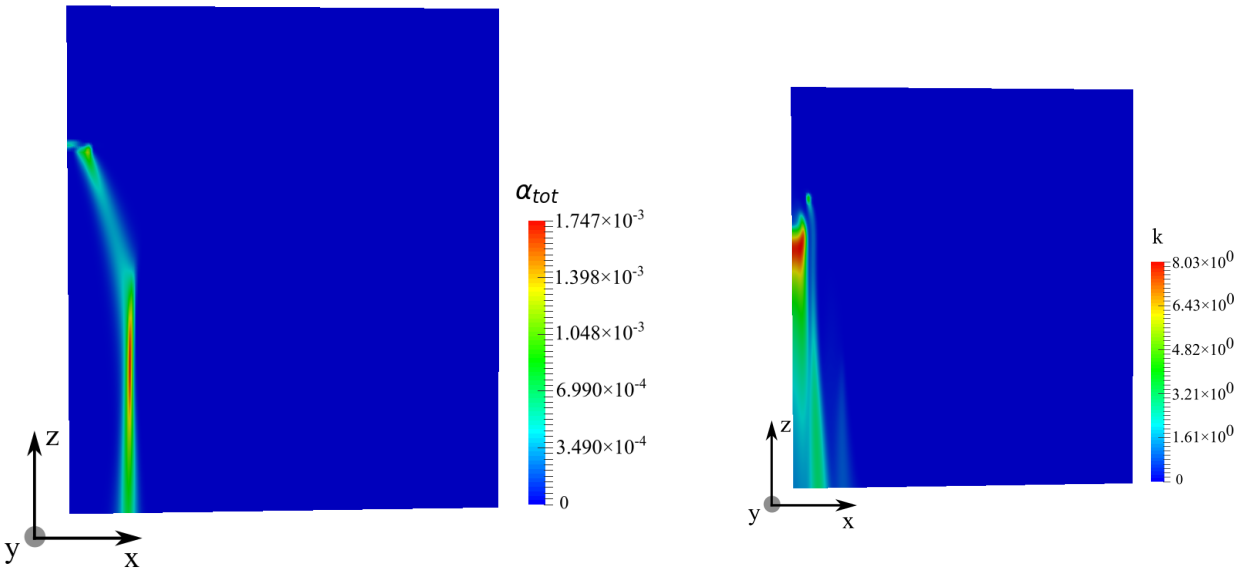

(**a**) (**b**)

Figure 8. Spatial distribution of the properties on XZ plane at $y = 0.05$ m for a monodisperse spray, $t = 10$ s, $\Delta x = 1.5$ cm, $\Delta t = 1$ ms; (**a**) droplet volume fraction α_{tot} and (**b**) turbulent kinetic energy k (m^2/s^2).

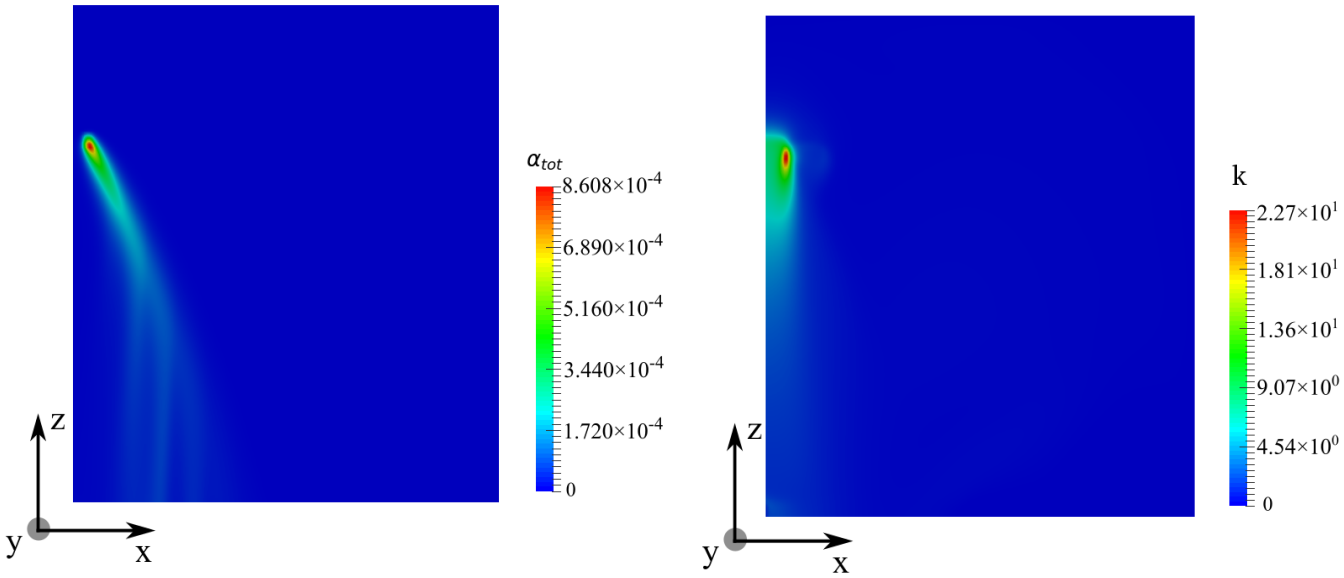

(**a**) (**b**)

Figure 9. Spatial distribution of the properties on XZ plane at $y = 0.05$ m for a polydisperse spray, $t = 10$ s, $\Delta x = 1.5$ cm, $\Delta t = 1$ ms; (**a**) droplet volume fraction α_{tot} and (**b**) turbulent kinetic energy k (m^2/s^2).

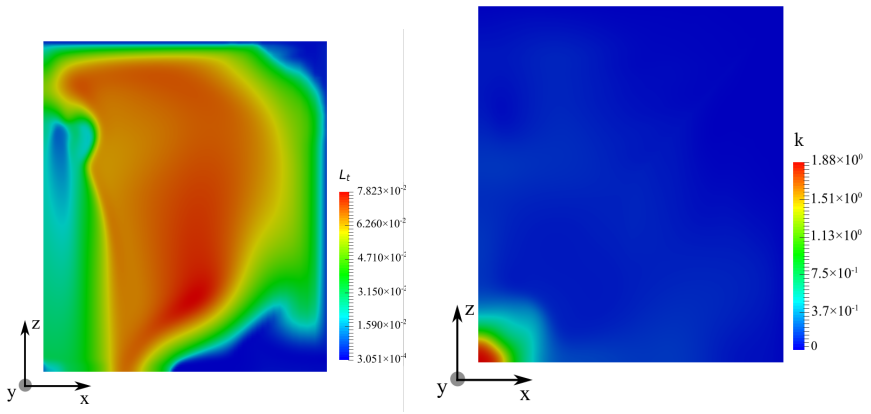

(**a**) (**b**)

Figure 10. (**a**) Turbulent integral length scale L_t (m) on the XZ plane at $y = 0.05$ m; (**b**) turbulent kinetic energy k (m^2/s^2) on the XY plane at $h = 1.5$ m.

Form Figure 10b, one can see that the turbulent kinetic energy is maximal around the symmetric axis of the geometry, in the center of the spray cone. The turbulent intensity seems to decrease with the radial distance R from the symmetric axis.

3.6.1. Droplet Volume Fraction

Figure 11 shows the evolutions of the normalized droplet volume fraction for different droplet classes. The distribution of droplet volume fraction α_{tot} at $h = 40$ cm is given in Figure 11a. One can see that the droplets of different diameters have almost the same radial distribution at $h = 40$ cm, where a maximal value at radial distance $R \approx 20$ cm is noted. However, for $h = 95$ cm, the maximal values separate for droplets of different diameters. Larger droplets show a maximal volume fraction at a radial distance farther than the small ones. This phenomena is due to the droplet inertia, i.e., with the same initial injection radial velocity, the large droplets need a larger distance to be decelerated by the drag force.

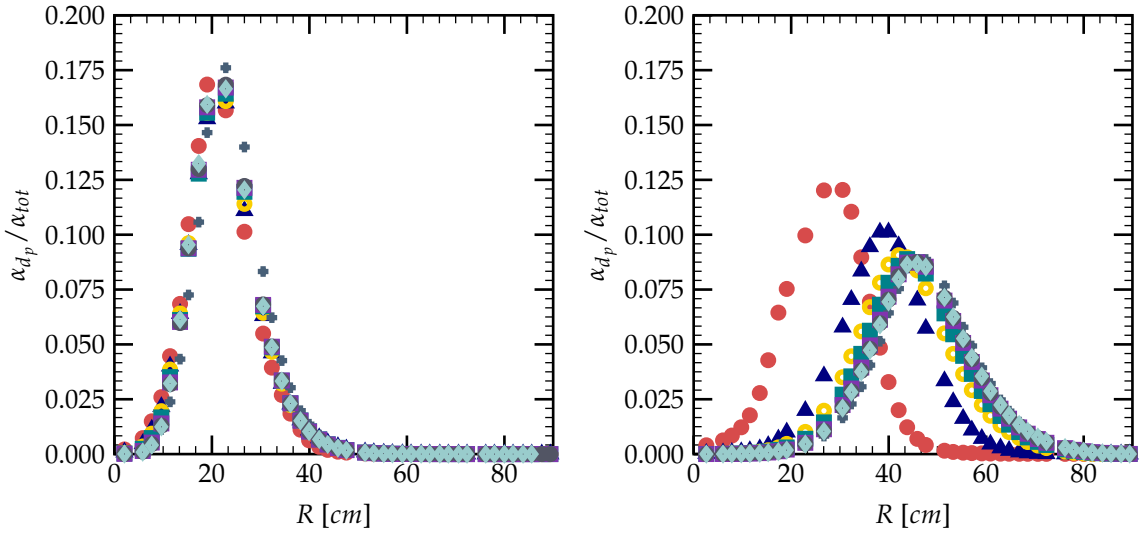

(**a**) (**b**)

Figure 11. Evolution of normalized volume fraction $\alpha_{d_p}/\alpha_{tot}$ for droplets of different diameters: $d_p = 166$ µm (●), $d_p = 277$ µm (▲), $d_p = 388$ µm (○), $d_p = 500$ µm (■), $d_p = 611$ µm (◆), $d_p = 722$ µm (□), $d_p = 833$ µm (●), $d_p = 944$ µm (◆); (**a**) $h = 40$ cm and (**b**) $h = 95$ cm.

3.6.2. Droplet Size Distribution

From another point of view, Figure 12 shows the histogram of normalized volume and number fractions for different droplets on vertical planes of $h = 20$ cm and $h = 95$ cm. These quantities can be important for the turbulence analysis since the spray bulk flow and droplet wake flow can both contribute to the turbulence generation in particle-laden flows [7,44]. One can see that at $h = 20$ cm, the droplets of diameter between 500 and 600 µm have the highest volume fraction compared to the droplets of other diameters in the polydisperse spray. However, smaller droplets of 300–400 µm are seen to be dominant in terms of the volume fraction at the plane $h = 95$ cm, as shown in Figure 12a. For the number fraction, one can see from Figure 12b that the small droplets of $d_p \approx 300$–400 µm are dominant at $h = 20$ cm in terms of droplet numbers. This domination is more significant for the planes farther from the nozzle, such as the plane of $h = 95$ cm. Thus, small droplets play a more important role in the zone far from the injection nozzle.

3.6.3. Surface-Averaged Volume Fraction

In order to study the vertical distribution of the droplet volume fraction below the spray nozzle, one can introduce the surface-averaged droplet volume fraction $\bar{\alpha}$ defined as:

$$\bar{\alpha} = \frac{\int_{S_{XY}} \alpha dS}{S_{XY}} \tag{9}$$

where S_{XY} is the surface of the plane orthogonal to the axis z, which has a constant value of 10 m^2 in the current geometry for single nozzle simulations.

One can note the evolution of $\bar{\alpha}$ as a function of the vertical distance h of the droplets along the z axis in Figure 13a. In both the monodisperse and the polydisperse cases, $\bar{\alpha}$ increases with the falling of the droplets. For the monodisperse case, $\bar{\alpha}$ increases and converges to a stable value of around 6×10^{-6}. The droplets fall with an initial velocity and accelerate as a result of the gravity, until $\bar{\alpha}$ reaches a constant value when the gravity reaches equilibrium with the gas friction. For the polydisperse case, one can see that $\bar{\alpha}$ keeps increasing, since for the droplets of large diameters, a larger equilibrium distance of the two forces on the droplets is required.

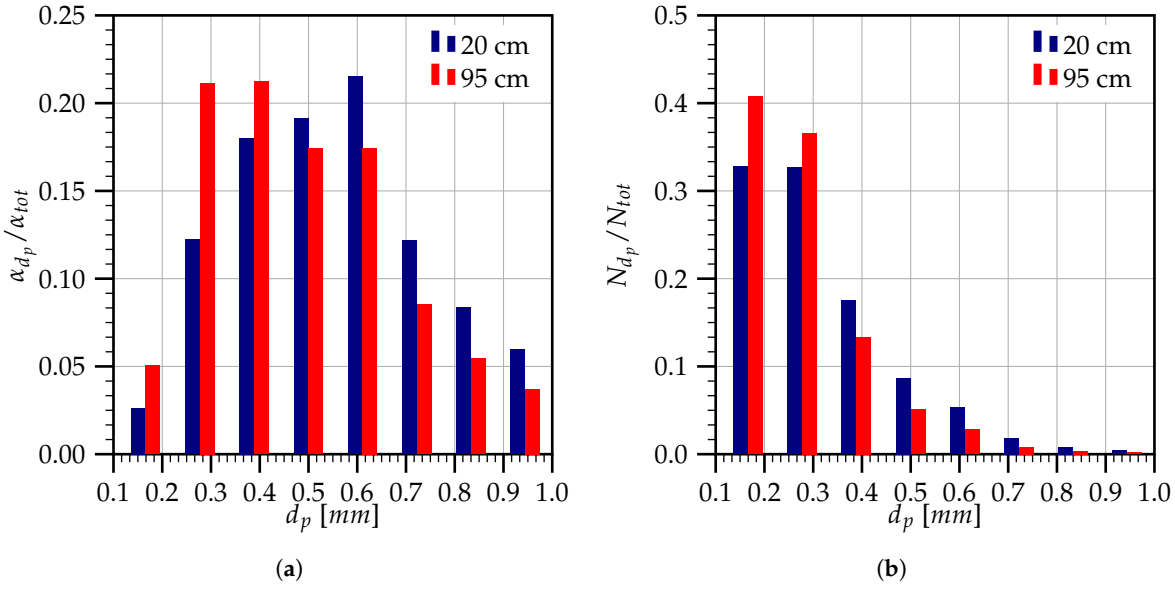

Figure 12. Histogram for different droplet diameters at vertical distances from the nozzle $h = 20$ cm and $h = 95$ cm; (**a**) normalized volume fraction $\alpha_{d_p}/\alpha_{tot}$ and (**b**) normalized number fraction N_{d_p}/N_{tot}.

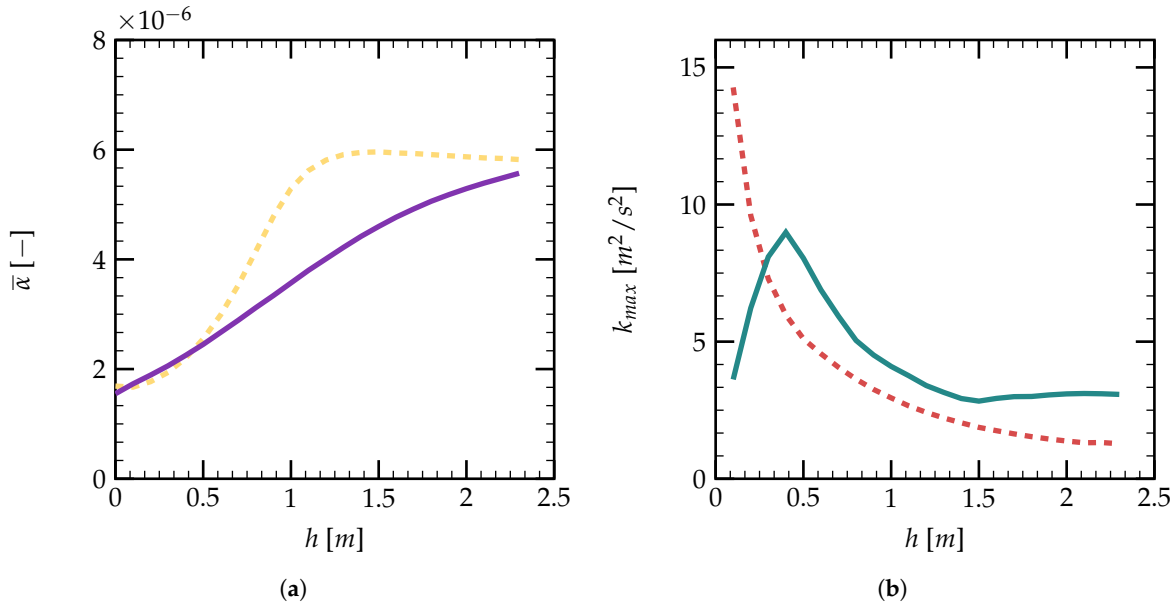

(**a**) (**b**)

Figure 13. (**a**) Evolution of the surface-averaged droplet volume fraction $\overline{\alpha}$ as a function of h; monodisperse spray (- - -), polydisperse spray (——); (**b**) Evolution of k_{max} at different vertical surfaces as a function of the vertical distance; monodisperse spray (——), polydisperse spray (- - -).

Figure 13b gives the evolution of the maximal turbulent kinetic energy k_{max} as a function of vertical distance h from the spray nozzle. For the polydisperse spray, the turbulent intensity decreases rapidly with the distance from the spray nozzle, which corresponds to Figure 10b. Two regions can be distinguished: within a distance $h < 1$ m from the nozzle, the turbulence intensity is relatively high, and for $h > 1$ m, the turbulent kinetic energy decreases to low values. Comparing to the monodisperse spray, the maximal value of k for the polydisperse spray is smaller for a vertical distance $h > 0.5$ m. As discussed above, the small droplets remain on the inner side of the spray cone, as depicted in Figure 11b. They have small inertia and can very quickly reach their terminal velocity, which is closely related to the turbulence intensity. From Figure 13a, one can see that the small droplets of 300 µm have reached their terminal velocities for $h > 1$ m. The dynamics of small droplets have important impacts on the turbulence intensity inside the spray cone.

4. Study of Two Interacting Nozzles

In this section, two interacting nozzles of polydisperse sprays are investigated numerically. Two polydisperse sprays are injected on the top of the geometry, as shown in Figure 14a, with a horizontal distance of 0.2 m between them. The injected spray droplets can form two hollow spray cones in the lower part. The two sprays have identical injection properties as defined in the polydisperse simulation, except for their positions. A mesh grid with mean mesh size $\Delta x = 2$ cm in the injection region was used for the simulation of the two-nozzle case, as depicted in Figure 14b. The simulation results on the XZ plane of $y = 0.05$ m are given in Figure 15.

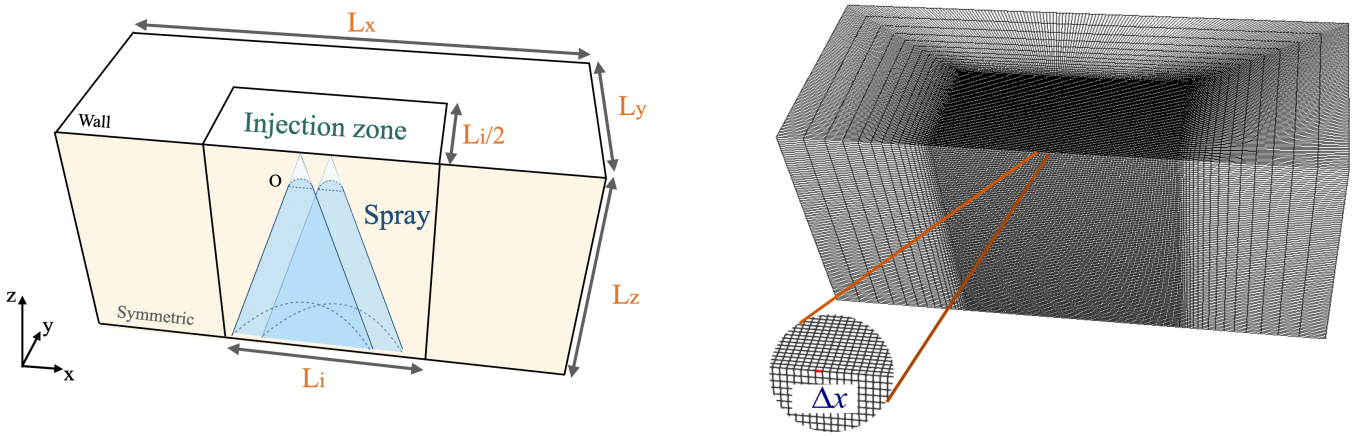

(**a**) (**b**)

Figure 14. (**a**) Geometry and (**b**) mesh of the two spray nozzles $\Delta x = 2$ cm; $L_i = 3$ m, $L_x = 7$ m, $L_y = 3$ m, and $L_z = 3.5$ m with O the numerical injection plane; symmetric and wall boundary conditions highlighted in (**a**).

Figure 15a shows the spatial droplet volume fraction distribution on the XZ plane. The spray droplets injected from two nozzles form an intersection region below the injection plane O. Generally, one can see that the droplet volume fraction α_{tot} decreases with the vertical distance. Figure 15b gives the evolution of the turbulence integral length scale in the case of two interacting sprays. Large droplets are noted to be important in numbers at the outer rim of the two spray cones. Similar to the single nozzle case, the turbulent kinetic energy k and the turbulent dissipation rate ε have high values inside the spray cones, as shown in Figure 15c,d. The droplet collision was considered; however, it is not the main contributor to the turbulence generation in this region. The droplet volume fraction in the interaction region is around $\mathcal{O}\left(10^{-4}\right)$, under which the collision probability can be quite small [10]. The TKE increase in this region is mainly due to the gas flow interaction induced by spray droplets' movements from the two different nozzles. For the lower region with $h > 1$ m, the turbulent kinetic energy k, as well as the dissipation rate decrease to a low value.

Figure 16 gives the evolutions of droplet volume fraction α_{tot} and turbulent kinetic energy k as a function of x on the XZ plane at $y = 0.05$ m. One can see that the interaction of the two polydisperse sprays begins for a vertical distance larger than $h = 0.2$ m. Figure 16a shows that the droplet volume fraction has three peaks at $h = 0.2$ m. The interaction zone has a higher value of α_{tot} than the spray cone generated from a single nozzle. The overall values for α_{tot} decrease with the vertical distance h, ranging from $\alpha_{tot} = 3.5 \times 10^{-4}$ to $\alpha_{tot} = 2 \times 10^{-5}$. One can see from Figure 16b that the interaction of the spray droplet can locally increase the TKE. Farther from the two spray nozzles, the TKE decreases with the vertical distance h. For $h > 1.0$ m, the distribution of the TKE becomes more homogeneous compared to the near-nozzle region.

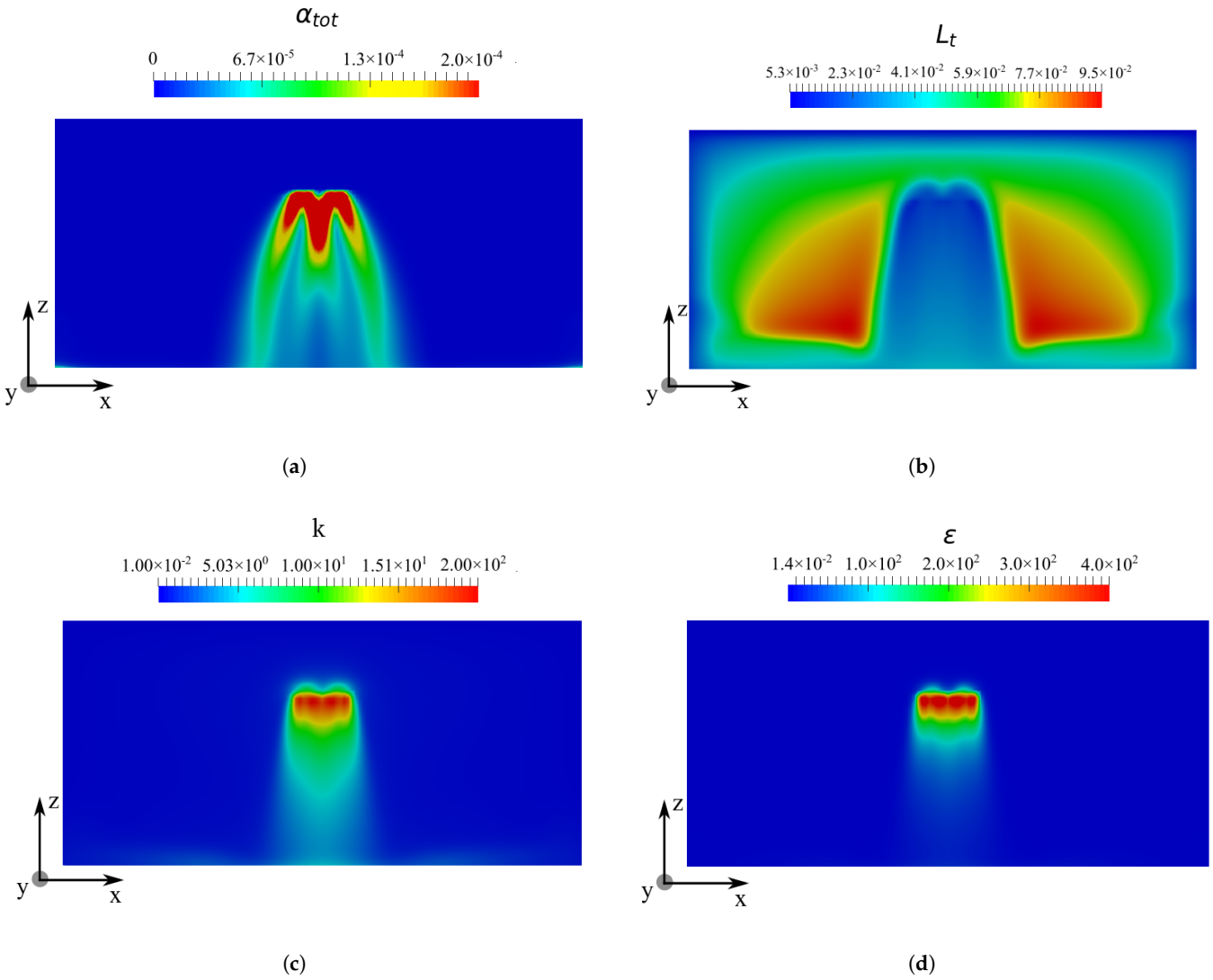

Figure 15. Properties on the XZ plane at 30 s; (**a**) droplet volume fraction α_{tot}, (**b**) integral length scale L_t (m), (**c**) turbulent kinetic energy k (m^2/s^2), and (**d**) turbulent dissipation rate ε (m^2/s^3).

Figure 17a,b shows the evolutions of the surface-averaged droplet volume fraction $\overline{\alpha}$ and maximal turbulent kinetic energy k_{max} on the XY plane as a function of h. In Figure 17a, $\overline{\alpha}$ increases linearly with h, as a result of the polydispersion of droplets generated from the two nozzles. The big droplets have not reached their terminal velocities in this range of vertical distance h. The value of $\overline{\alpha}$ is noted to be larger than the single nozzle case shown in the dark blue dashed line. Figure 17b gives the evolution of k_{max} on the z direction, which has an analogous trend as the polydisperse spray out of a single nozzle. k_{max} has similar values near the spray nozzles; however, one can have a higher value for k_{max} for the two-nozzle case than the case of a single nozzle in the far-from-the-nozzle region. This can be due to the fact that the water injection rate is doubled in the two-nozzle case.

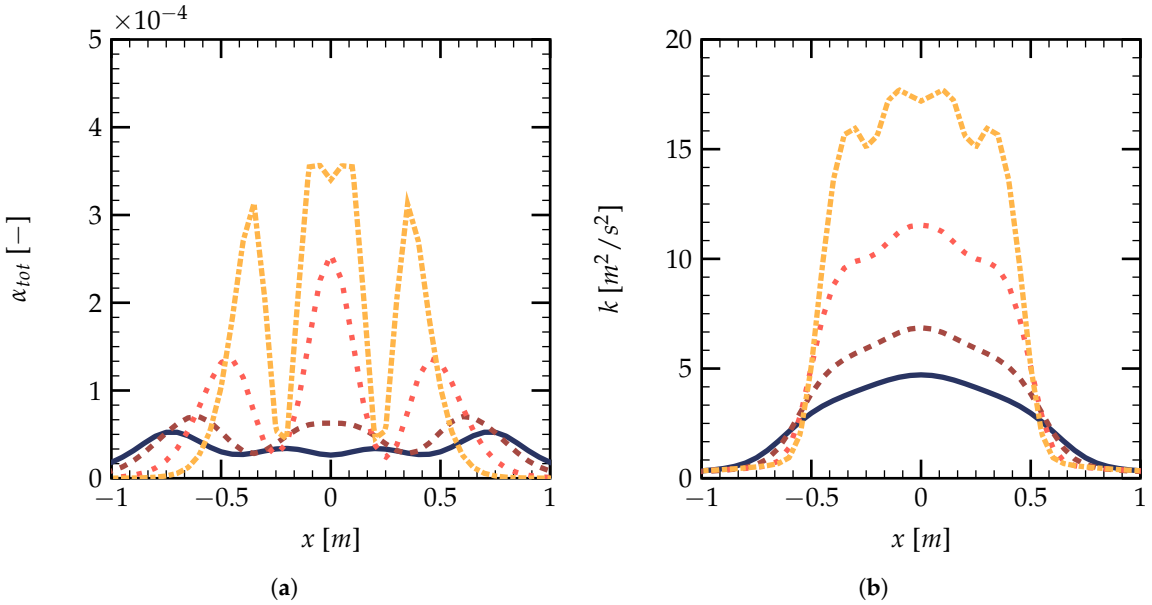

Figure 16. Evolutions of the droplet volume fraction α_{tot} (**a**) and the turbulent kinetic energy k (m^2/s^2) (**b**) on the XY plane $y = 0.05$ m as a function of x, $h = 0.2$ m (——), $h = 0.5$ m (· · ·), $h = 1.0$ m (– – –), and $h = 1.5$ m (——).

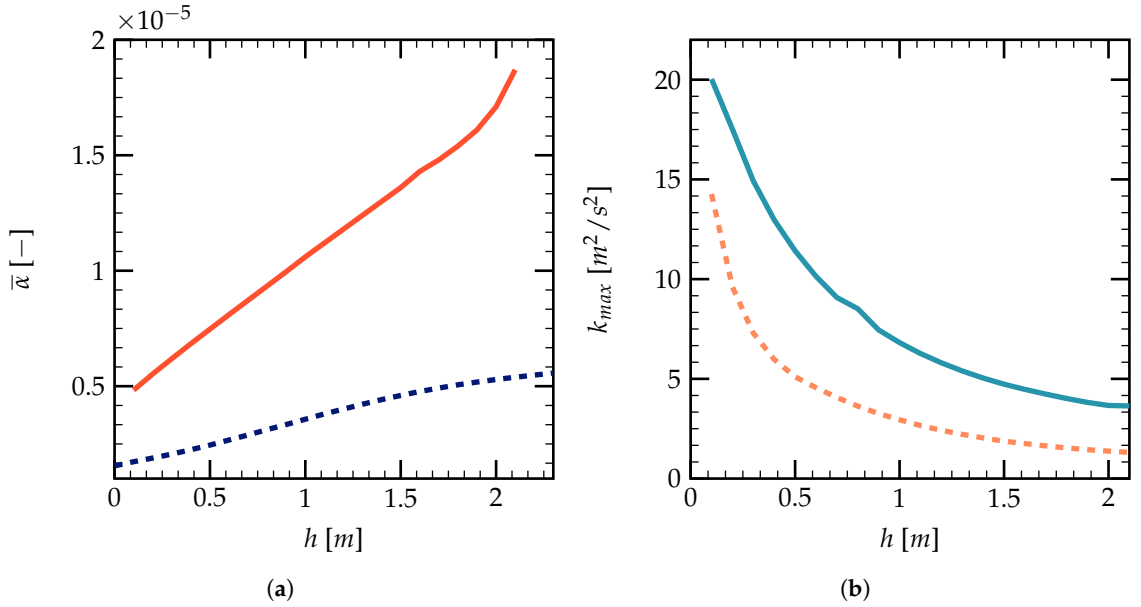

Figure 17. (**a**) Evolution of the surface averaged droplet volume fraction $\overline{\alpha}$ as a function of h: tow nozzles (——) and single nozzle (– – –); (**b**) evolution of k_{max} as a function of the vertical distance h: two nozzles (——) and single nozzle (– – –).

5. Conclusions and Perspectives

The spray-induced turbulence generated from industrial nozzles is investigated numerically using an RANS turbulence model. Water sprays injected from a single nozzle, as well as two interacting nozzles are studied both qualitatively and quantitatively. The polydisperse model is proven to be more accurate than the monodisperse one for the evaluation of the gas and droplet velocities. In both the single- and two-nozzle cases, the spray-induced turbulence is noted to be more intense inside the spray cone. The turbulent kinetic energy inside a polydisperse spray seems to be lower than the monodisperse case since the small droplets locate on the inner rim of the polydisperse spray cone, which can diminish the turbulence intensity. The turbulent kinetic energy decreases with the vertical distance from the nozzle, which maintains a low value for a distance larger than

1 m. For large-scale simulations, the near-nozzle region and far-from-the-nozzle region can be simulated separately, since the turbulent properties in the latter region are more homogenous. Comparing the single- and two-nozzle cases, the far-field turbulence intensity is larger with a higher water injection rate. However, the collisions of the droplets have small impacts on the turbulence generation as a result of the low droplet volume fraction in the interaction region. Future studies can be carried out on the effects of water spray on explosive gas-air mixing. The droplet collision effects can be important for nozzles with higher water injection rates.

Author Contributions: Conceptualization, G.G., S.K., and S.M.; methodology, S.K. and A.H.; software, G.G. and S.M.; validation, G.G., S.K., and O.T.; formal analysis, G.G. and O.T.; investigation, G.G. and S.K.; resources, G.G. and S.M.; data curation, G.G., O.T., and S.M.; writing—original draft preparation, G.G. and S.K.; writing—review and editing, S.M., O.T., and A.H.; visualization, G.G. and S.K.; supervision, S.K., A.H., and O.T.; project administration, A.H.; funding acquisition, S.K. All authors read and agreed to the published version of the manuscript.

Funding: This research was funded by Accord Tripartie CEA/EDF/Framatome Institut 2020—F35158.

Institutional Review Board Statement: Not applicable.

Informed Consent Statement: Not applicable.

Data Availability Statement: The data that support the findings of this study are available from the corresponding author upon request.

Acknowledgments: The authors gratefully acknowledge the financial support from Electricité de France (EDF) within the framework of the Generation II & III reactor research program.

Conflicts of Interest: The authors declare no conflict of interest.

Abbreviations

d_p	Droplet diameter
f_g	Gravity acceleration
h	Vertical distance from the spray nozzle
h_κ	Phase-averaged specific enthalpy for phase κ
k_{max}	Maximal turbulent kinetic energy
L_x, L_y, L_z	Geometry sizes
L_t	Turbulence integral length scale
M	Interphase momentum transfer term
N_{d_p}	Number of droplets of diameter d_p
p	Gas pressure
Pa	Droplet momentum number
q	Heat transfer flux
R	Radius from spray cone center
$R_{i,j}$	Reynolds stress
u_g	Gas velocity
v_p	Particle velocity
α_{tot}	Total volume fraction of droplets
$\overline{\alpha}$	Surface-averaged droplet volume fraction
ρ	Mass density
ε	Turbulent dissipation rate
Γ	Interphase mass transfer rate
Δ_t	Time step
Δ_x	Grid size
DNS	Direct Numerical Simulation
RANS	Reynolds-Averaged Navier–Stokes
LES	Large Eddy Simulation
TKE	Turbulent Kinetic Energy

References

1. Landahl, H.; Herrmann, R. Sampling of liquid aerosols by wires, cylinders, and slides, and the efficiency of impaction of the droplets. *J. Colloid Sci.* **1949**, *4*, 103–136. [CrossRef]
2. Thomas, G. On the conditions required for explosion mitigation by water sprays. *Process. Saf. Environ.* **2000**, *78*, 339–354. [CrossRef]
3. Gai, G.; Kudriakov, S.; Hadjadj, A.; Studer, E.; Thomine, O. Modeling pressure loads during a premixed hydrogen combustion in the presence of water spray. *Int. J. Hydrogen Energy* **2019**, *44*, 4592–4607. [CrossRef]
4. Kudriakov, S.; Dabbene, F.; Studer, E.; Beccantini, A.; Magnaud, J.; Paillère, H.; Bentaib, A.; Bleyer, A.; Malet, J.; Porcheron, E.; et al. The TONUS CFD code for hydrogen risk analysis: Physical models, numerical schemes and validation matrix. *Nucl. Eng. Des.* **2008**, *238*, 551–565.
5. Wingerden, K.; Wilkins, B. The influence of water sprays on gas explosions. Part 2: Mitigation. *J. Loss Prevent. Proc.* **1995**, *8*, 61–70. [CrossRef]
6. Gai, G.; Kudriakov, S.; Rogg, B.; Hadjadj, A.; Studer, E.; Thomine, O. Numerical study on laminar flame velocity of hydrogen-air combustion under water spray effects. *Int. J. Hydrogen Energy* **2019**, *44*, 17015–17029. [CrossRef]
7. Wingerden, K.; Wilkins, B. The influence of water sprays on gas explosions. Part 1: Water-spray-generated turbulence. *J. Loss Prevent. Proc.* **1995**, *8*, 53–59. [CrossRef]
8. Hetsroni, G.; Sokolov, M. Distribution of mass velocity and intensity of turbulence in a two-phase turbulent jet. *ASME J. Appl. Mech.* **1971**, *38*, 315–327. doi:10.1115/1.3408779. [CrossRef]
9. Hetsroni, G. Particles-turbulence interaction. *Int. J. Multiph. Flow* **1989**, *15*, 735–746. [CrossRef]
10. Elghobashi, S. On predicting particle-laden turbulent flows. *Appl. Sci. Res.* **1994**, *52*, 309–329. [CrossRef]
11. Sadiki, A.; Chrigui, M.; Janicka, J.; Maneshkarimi, M.R. Modeling and simulation of effects of turbulence on vaporization, mixing and combustion of liquid-fuel sprays. *Flow Turbul. Combust.* **2005**, *75*, 105–130. [CrossRef]
12. Mallouppas, G.; George, W.; van Wachem, B. Dissipation and inter-scale transfer in fully coupled particle and fluid motions in homogeneous isotropic forced turbulence. *Int. J. Heat. Fluid Flow* **2017**, *67*, 74–85. [CrossRef]
13. Gadalla, M.; Kannan, J.; Tekgül, B.; Karimkashi, S.; Kaario, O.; Vuorinen, V. Large-eddy simulation of ECN spray A: Sensitivity study on modeling assumptions. *Energies* **2020**, *13*, 3360. [CrossRef]
14. Crowe, C.; Schwarzkopf, J.; Sommerfeld, M.; Tsuji, Y. *Multiphase Flows with Droplets and Particles*; CRC, Taylor and Francis: Boca Raton, FL, USA, 2012; ISBN 9781439840504.
15. Gai, G.; Hadjadj, A.; Kudriakov, S.; Thomine, O. Particles-induced turbulence: A critical review of physical concepts, numerical modelings and experimental investigations. *Theor. App. Mech. Lett.* **2020**, *10*, 1–7. [CrossRef]
16. Gore, R.; Crowe, C. Modulation of turbulence by a dispersed phase. *ASME J. Fluids Eng.* **1991**, *113*, 304–307. [CrossRef]
17. Gore, R.; Crowe, C. Effect of particle size on modulating turbulent intensity. *Int. J. Multiph. Flow* **1989**, *15*, 279–285. [CrossRef]
18. Tanaka, T.; Eaton, J. Sub-Kolmogorov resolution particle image velocimetry measurements of particle-laden forced turbulence. *J. Fluid Mech.* **2010**, *643*, 177–206. [CrossRef]
19. Lefebvre, A.; McDonell, V.G. *Atomization and Sprays*; CRC, Taylor and Francis: Boca Raton, FL, USA, 2016.
20. Kim, K.; Lim, O. Investigation of the spray development process of gasoline-biodiesel blended fuel sprays in a constant volume chamber. *Energies* **2020**, *13*, 4819. [CrossRef]
21. Foissac, A. Modélisation des Interactions Entre Gouttes en Environnement Hostile. Ph.D. Thesis, Université Pierre & Marie Curie, Paris, France, 2011.
22. Keser, R.; Ceschin, A.; Battistoni, M.; Im, H.; Jasak, H. Development of a eulerian multi-fluid solver for dense spray applications in OpenFOAM. *Energies* **2020**, *13*, 4740. [CrossRef]
23. Mimouni, S.; Lamy, J.S.; Lavieville, J.; Guieu, S.; Martin, M. Modeling of sprays in containment applications with A CMFD code. *Nucl. Eng. Des.* **2010**, *240*, 2260–2270. [CrossRef]
24. Elghobashi, S.; Balachandar, S.; Prosperetti, A. An updated classification map of particle-Laden turbulent flows. *IUTAM Symp. Comput. Approaches Multiph. Flow* **2006**, *81*, 3–10.
25. Yuan, Z.; Michaelides, E. Turbulence modulation in particulate flows. A theoretical approach. *Int. J. Multiph. Flow* **1992**, *18*, 779–785. [CrossRef]
26. Yarin, L.; Hetsroni, G. Turbulence intensity in dilute two-phase flows -3 The particles-turbulence interaction in dilute two-phase flow. *Int. J. Multiph. Flow* **1994**, *20*, 27–44. [CrossRef]
27. Wacks, D.H.; Chakraborty, N. Flame structure and propagation in turbulent flame-droplet interaction: A direct numerical simulation analysis. *Flow Turbul. Combust.* **2016**, *96*, 1053–1081. [CrossRef]
28. Crowe, C. On models for turbulence modulation in fluid-particle flows. *Int. J. Multiph. Flow* **2000**, *26*, 719–727. [CrossRef]
29. Mandø, M. Turbulence Modulation by Non-Spherical Particles. Ph.D. Thesis, Aalborg Universitet, Aalborg, Denmark, 2009.
30. Mandø, M.; Lightstone, M.; Rosendahl, L.; Yin, C.; Sørensen, H. Turbulence Modulation in Dilute Particle-Laden Flow. *Int. J. Heat. Fluid Flow* **2009**, *30*, 331–338. [CrossRef]
31. Elghobashi, S. Direct numerical simulation of turbulent flows laden with droplets or bubbles. *Annu. Rev. Fluid Mech.* **2019**, *51*, 217–244. [CrossRef]
32. Banerjee, S.; Rutland, C. Study of spray induced turbulence using large eddy simulations. *At. Sprays* **2015**, *25*, 285–316. [CrossRef]

33. Gexcon, A.S. FLACS Code User Manual. 2020. Available online: http://www3.gexcon.com/files/manual/flacs/html/index.html (accessed on 12 November 2020).
34. Khan, M.; Zou, R.; Yu, A. Computational simulation of air-side heat transfer and pressure drop performance in staggered mannered twisted oval tube bundle operating in crossflow. *Int. J. Therm. Sci.* **2021**, *161*, 106748. [CrossRef]
35. Thomine, O. Development of Multi-Scale Methods for the Numerical Simulation of Biphasic Reactive Flows. Ph.D. Thesis, University of Rouen, Mont-Saint-Aignan, France, 2011.
36. Mimouni, S.; Boucker, M.; Laviéville, J.; Guelfi, A.; Bestion, D. Modeling and computation of cavitation and boiling bubbly flows with the NEPTUNE_CFD code. *Nucl. Eng. Des.* **2008**, *238*, 680–692. [CrossRef]
37. *Neptune_CFD Version 4.3.1 Theory Guide*; EDF: Paris, France, 2019.
38. Ishii, M.; Hibiki, T. *Thermo-Fluid Dynamics of Two-Phase Flow*; Springer: Berlin, Germany, 2006.
39. Pironneau, O.; Mohammadi, B. *Analysis of the k-Epsilon Turbulence Model*; Mason: Paris, France, 1994.
40. Mimouni, S. Modeling and cavitation flows: A two-phase flow approach. *La Houille Blanche* **2006**, *6*, 121–128. [CrossRef]
41. Lechler. *Precision Spray Nozzles and Engineered Solutions for the Chemical Industry*; Technical Report; Lechler: Metzingen, Germany, 1996.
42. Foissac, A.; Malet, J.; Vetrano, R.; Buchlin, J.; Mimouni, S.; Feuillebois, F.; Simonin, O. Experimental measurements of droplet size and velocity distributions at the outlet of a pressurized water reactor containment swirling spray nozzle. In Proceedings of the XCFD4NRS-3, Bethesda, MD, USA, 14–16 September 2010.
43. Foissac, A.; Sestier-Carlin, R.; Malet, J. *Dimensionnement du Banc CALIST*; Rapport IRSN/DSU/SERAC/LEMAC/10-28; IRSN: Paris, France, 2010.
44. Risso, F. Agitation, mixing, and transfers induced by bubbles. *Annu. Rev. Fluid Mech.* **2018**, *50*, 25–48. [CrossRef]